DOI: https://doi.org/10.2138/am-2019-6674

Revision 1

Trace element distributions in (Cu)-Pb-Sb sulfosalts from the Gutaishan Au–Sb deposit, South China: Implications for formation of high-fineness native gold

WEI LI[1,2], NIGEL J. COOK[3], CRISTIANA L. CIOBANU[3], GUIQING XIE[1,*], BENJAMIN P. WADE[4], SARAH E. GILBERT[4]

[1]Key Laboratory of Metallogeny and Mineral Assessment, Institute of Mineral Resources,
Chinese Academy of Geological Sciences, Beijing 100037, China

[2]Faculty of Earth Resources, China University of Geosciences, Wuhan 430074, China

[3]School of Chemical Engineering, The University of Adelaide, 5005 S.A., Australia

[4]Adelaide Microscopy, The University of Adelaide, 5005 S.A., Australia

ABSTRACT

Compositional data, comprising electron probe microanalysis and laser-ablation inductively coupled plasma mass spectrometry (LA-ICP-MS) trace element data are presented for common (Cu)-Pb-Sb sulfosalts (bournonite, jamesonite, tetrahedrite and boulangerite), subordinate semseyite, heteromorphite, robinsonite and (Cu)-Pb-Bi-Sb sulfosalts, and for accompanying base metal sulfides (BMS) in auriferous gold veins from the Gutaishan Au–Sb deposit, southern China. The objectives of the study were to: identify whether these sulfosalts represent overlooked hosts for precious metals and other trace elements of petrogenetic or economic interest; establish partitioning trends among co-existing sulfosalt species and between sulfosalts and BMS; and to seek evidence for a genetic link between the abundance of (Cu)-Pb-Sb sulfosalts and the high-fineness of native gold in the deposit. All (Cu)-Pb-Sb sulfosalts analyzed were found to be remarkably poor hosts for gold and thus do not contribute to the overall mineralogical

---

[*] Corresponding author E-mail address: xieguiqing@cags.ac.cn

balance for gold. Trace yet measurable concentrations of Au are, however, noted in the (Cu)-Pb-Bi-Sb sulfosalts, in agreement with published data indicating that (Cu)-Pb-Bi-Sb sulfosalts may be minor Au-hosts in some ore systems. Silver is preferentially partitioned into tetrahedrite at the expense of other sulfosalt phases, and tetrahedrite is thus the major host for Ag in the Gutaishan deposit. LA-ICP-MS trace element mapping allows partitioning relationships among different sulfosalt and BMS phases to be determined for several trace elements. Jamesonite concentrates Fe, Zn, Bi, Cd, Ag, Ni, and In over co-existing bournonite, yet boulangerite is the better host for As, Ag, Sn, Se and Te than jamesonite. Cadmium and Co are typically enriched in sphalerite relative to any sulfosalt, and when present, pyrite is always enriched in Au and Co relative to all other phases. A high Au/Ag ratio in the ore-forming fluid, the presence of abundant tetrahedrite that has sequestered silver during mineral precipitation, and a lack of evidence for cooling-driven precipitation may be significant reasons for the formation of high-fineness gold throughout the deposit. Two generations of native gold are documented whereby the first is coarse-grained, Ag- and Bi-bearing, and is associated with the main (Cu)-Pb-Sb sulfosalts, bournonite, jamesonite, tetrahedrite and boulangerite). The second generation is fine-grained and has the highest fineness. Increase in the complexity of sulfosalt assemblages, re-distribution of Ag within coarse native gold and dissolution-reprecipitation reactions among the sulfosalt-gold association increase the gold fineness. The present study shows that linking petrographic aspects at the micrometer-scale with minor/trace element distributions in complex sulfide-sulfosalt assemblages can track a complex history of Au deposition and enrichment.

Keywords: Sulfosalts, trace elements, high-fineness native gold, gold deposits, Gutaishan

---

INTRODUCTION

In recent years, significant progress has been made in understanding the role played by different common sulfide minerals in controlling the distributions of precious metals and other potentially economic components within ores of different types (Cook and Chryssoulis 1990; Abraitis et al. 2004; Cook et al. 2009, 2013; George et al. 2015, 2017, 2018). Furthermore, evidence has accumulated to show preferential partitioning of key trace elements among the most common sulfide minerals (chalcopyrite, sphalerite and galena) where they precipitated in equilibrium (George et al. 2016).

Sulfosalts are a large family of minerals, containing more than 220 valid mineral species at the time of the most recent review (Moëlo et al. 2008), with numerous additional species discovered since this publication appeared. Although many sulfosalt minerals are exceedingly rare, Cu-Pb-Sb, Pb-Sb and (Cu)-Pb-Bi-Sb sulfosalts are relatively common components in a wide variety of Au-Ag-bearing ore deposits, where they commonly display a close paragenetic association with native gold (e.g., Wagner and Jonsson 2001; Cook and Ciobanu 2004; Fadda et al. 2005; Ciobanu et al. 2009; 2016, and reference therein). A genetic relationship between gold and various bismuth minerals is now widely accepted based on both empirical and experimental data supporting the bismuth scavenger model (Tooth et al. 2008; Ciobanu et al. 2009, 2016). Ciobanu et al. (2009) have shown that certain Pb-Bi sulfosalts can contain up to several thousands of ppm Au. In contrast, however, remarkably little is known about the capacity of Sb-dominant sulfosalts, apart from the better studied tetrahedrite group, to host Au and Ag, or indeed the concentrations of a broader range of trace elements that may potentially be accommodated within their structures (Sack and Loucks 1985; George et al. 2017), even though the association of gold with (Cu)-Pb-Sb sulfosalts is well established and documented.

The Au–Sb deposits in central Hunan Province represent one of the most important Sb–Au metallogenic belts in China (Hu and Zhou 2012; Mao et al. 2013; Hu et al. 2017; Xie et al. 2018). The belt hosts more than 170 Sb and Au deposits and prospects (Hu et al. 2017), including the world's largest Sb deposit (Xikuangshan), the Gutaishan Au–Sb deposit, and the Longshan Sb–Au deposit. These are characterized by native gold of high fineness and an abundance of (Cu)-Pb-Sb sulfosalts, notably bournonite (Peng et al. 2000; Zhu and Peng 2015, and this study). The mineralogy and paragenesis of these sulfosalts and their role in ore formation have received scant prior attention in the literature.

This contribution focuses on the slate-hosted Gutaishan Au–Sb deposit, the highest-grade gold deposit in central Hunan Province (Li et al. 2016, in press). Systematic mineralogical and petrographic textural examination shows that an abundance of (Cu)-Pb-Sb sulfosalts and subordinate (Cu)-Pb-Bi-Sb sulfosalts, together with minor base metal sulfides (sphalerite, galena and chalcopyrite; BMS), occur in close paragenetic association with native gold. Based on compositional data from electron probe microanalysis (EPMA) and laser-ablation inductively coupled plasma mass spectrometry (LA-ICP-MS), our aim is to: (1) understand whether the sulfosalts are potential, hitherto-overlooked hosts for precious metals and other trace elements of interest; (2) establish partitioning trends among co-existing sulfosalt species and between sulfosalts and BMS; and (3) provide evidence for a genetic link between high-fineness native gold and sulfosalts.

THE GUTAISHAN AU–SB DEPOSIT

The slate-hosted Gutaishan lode Au–Sb deposit, located in central Hunan Province, contains proven reserves of 9 tonnes Au and 2,500 tonnes Sb and is notable for its very high gold grade (Li et al. 2016). Although the average grade is about 13 g/t Au, bonanza grade ores can locally contain as much as 10,000 g/t Au (Li et al. 2016, Li et al. in press). No intrusive rocks are exposed at the surface or intersected by drilling but hidden intrusions have been inferred at depth within the mining district based on the interpretation of geophysical data (Rao et al. 1993). Arsenopyrite and pyrite are the main sulfides within the auriferous quartz veins and host up to several to hundreds of ppm ‘invisible gold’ (Li et al. in press). The veins also contain different species of (Cu)-Pb-Sb sulfosalts, minor BMS, scarce (Cu)-Pb-Bi-Sb sulfosalts and Bi-tellurides (Fig. 1). The occurrence of macroscopic sulfosalts can be a good indicator for high-grade or bonanza-grade gold ores, as they are often accompanied by an abundance of coarse-grained native gold.

SAMPLING AND METHODOLOGY

Representative samples were collected from the Gutaishan Au–Sb deposit and prepared as one-inch-diameter polished blocks. These are described in detail by Li et al. (in press). The analytical work reported here was carried-out on a sub-set of seven samples with particularly abundant sulfosalts.

All analytical work was performed at Adelaide Microscopy, The University of Adelaide. Samples were initially examined under a Leitz Laborlux-12-Pol dual reflected-transmitted light polarizing microscope and FEI QUANTA-450 scanning electron microscope (SEM). EPMA data for sulfosalts and BMS were collected using a Cameca SX-Five Electron Probe Microanalyser, equipped with five WDS X-Ray detectors. All measurements were performed at an accelerating voltage of 20 kV, beam current of 20 nA, and beam size of 1 μm. Peak/back ground positions, count times, reference standards and average minimum limits of detection (mdl) are listed in Supplemental[1]. Calibration and data reduction was carried-out in Probe for EPMA, distributed by Probe Software Inc.

LA-ICP-MS spot analysis and element mapping of sulfosalts and BMS were performed using a 213 nm, Q-switched, Nd: YAG New Wave NWR213 laser ablation system and coupled to an Agilent 7900 Quadrupole ICP-MS instrument. Operating conditions, measured isotopes, and data processing routines are given in Supplemental[1].

PETROGRAPHY OF SULFOSALT-BMS ASSEMBLAGES

The following sulfosalt species are identified in approximate order of abundance: bournonite ($PbCuSbS_3$); tetrahedrite [$Cu_{10}(Fe,Zn)_2Sb_4S_{13}$]; jamesonite ($Pb_4FeSb_6S_{14}$); boulangerite ($Pb_5Sb_4S_{11}$); semseyite ($Pb_9Sb_8S_{21}$); heteromorphite ($Pb_7Sb_8S_{19}$); and robinsonite ($Pb_4Sb_6S_{13}$). (Cu)-Pb-Bi-Sb sulfosalts, galena, native bismuth and Bi-tellurides are additional minor components in Au-rich samples found as stringers in the quartz veins without (Cu)-Pb-Sb sulfosalts. Simultaneous precipitation of sulfosalts and native gold is strongly supported by textural observations at the micrometer-scale (Fig. 2). Galena, chalcopyrite and sphalerite, in different proportions, coexist with, and are intergrown with sulfosalts (Figs. 1a, 1c, 1e, and 2a, 2f). Native gold occurs as coarser, lobate grains (Au1) and as interstitial, fine-grained aggregates (Au2) intergrown with gangue and/or other phases (Figs. 2a–2b and 2g).

Bournonite is the most common sulfosalt and occurs as patches randomly distributed within quartz veins (Fig. 1a). On backscatter electron (BSE) images, coarse-grained bournonite (hundreds to thousands of μm in size) are commonly intergrown with or enclose other minerals (e.g. jamesonite) (Figs. 2a–2d). Tetrahedrite is largely restricted to portions of the veins containing chalcopyrite, with which it is closely associated (Fig. 1c). Tetrahedrite is observed to be intergrown with native gold, bournonite, sphalerite and galena, but is clearly replaced by chalcopyrite (Fig. 2a).

Boulangerite occurs as relatively coarse felt-like masses and prismatic crystals intergrown with bournonite and jamesonite (Figs. 1b and 1e). Two distinct textural types are recognized: boulangerite as isolated, generally prismatic grains (Fig. 2e), and anhedral boulangerite along the margins of bournonite (Figs. 2b–2c) or marking the grain boundary between jamesonite and sphalerite. Robinsonite is observed as fine, acicular crystals enclosed in bournonite (Fig. 2c). Jamesonite is largely present as irregularly-shaped inclusions within bournonite (Figs. 2b–2d), or irregularly at grain boundaries between boulangerite and sphalerite. In addition, other minor/trace sulfosalts occur along the mutual boundaries between main components such as jamesonite and bournonite (Figs. 2b and 2d). These include semseyite, heteromorphite, and an additional unidentified Pb-Sb-S phase, all of which show differences in habit (Fig. 2d). Elongate grains of heteromorphite are intergrown with anhedral semseyite. The unidentified Pb-Sb-S phase shows a close association with heteromorphite. Although clearly distinct from other (Cu)-Pb-Sb sulfosalts, stoichiometry could not be accurately measured due to small size.

Trace (Cu)-Pb-Bi-Sb sulfosalts occur within small patches in some quartz veins that notably lack (Cu)-Pb-Sb sulfosalts (Fig. 1d). At least two distinct (Cu)-Pb-Bi-Sb sulfosalts are identified: an intermediate member of the giessenite-izoklakeite series; and kobellite. These are conspicuous by their intimate coexistence with native gold, galena, trace native bismuth and Bi-tellurides. The crystal chemistry of these phases is beyond the scope of the present manuscript and will be reported elsewhere.

COMPOSITIONAL DATA

Compositional data (EPMA and LA-ICP-MS) for sulfosalts and BMS are summarized in Tables 1 and 2; full datasets can be found as Supplemental[2] Tables S1 and S2.

Major element data

Bournonite is compositionally homogeneous with respect to major elements, S, Pb, Cu and Sb, with only limited solid solution towards seligmannite, $PbCuAsS_3$ (0.11 to 1.34 wt% As). The general chemical formula, based on 3 sulfur atoms per formula unit (apfu), can be expressed as: $Pb_{0.96–0.99}Cu_{1.00–1.03}Sb_{0.92–1.02}As_{0.00–0.09}S_{2.94–3.01}$. Concentrations of other elements are mainly below mdl.

Tetrahedrite compositions are As-poor in all analyzed samples, with wt% As values varying from 0.41 to 2.88, i.e., limited solid solution away from end-member tetrahedrite. Analyzed grains are Zn-Fe dominant: 5.16 to 7.42 wt% Zn; and 0.48 to 3.07 wt% Fe, respectively. The average empirical formula for tetrahedrite based on 13 S apfu is: $Cu_{9.60–10.03}Fe_{0.14–0.88}Zn_{1.27–1.86}As_{0.09–0.62}Sb_{3.29–3.81}S_{12.97–13.39}$.

Boulangerite displays a very limited range of compositions. Arsenic, Cu, Fe are either below mdl or up to 0.93, 0.32, and 0.18 wt%, respectively. The contents of Bi show relatively larger ranges, from below mdl to 0.68 wt%, displaying inverse correlation with the content of Sb. A generalized formula based on 11 S apfu can be expressed as: $Pb_{4.90–4.97}Cu_{0.00–0.09}Fe_{0.00–0.06}Sb_{3.88–4.14}As_{0.15–0.24}S_{10.65–10.80}$.

Jamesonite contains measurable Bi, Cu, and Zn, ranging from <mdl to 0.60 wt%, 0.04 to 0.17 wt%, and <mdl to 0.08 wt%, respectively. Major element concentrations are consistent with limited substitution of As for Sb. An average empirical formula based on 14 S apfu can be calculated as: $Pb_{3.79–3.87}Fe_{0.88–0.97}Cu_{0.01–0.06}Sb_{5.91–6.06}As_{0.19–0.24}S_{13.82–14.01}$.

Robinsonite has limited compositional variance with respect to S, Pb and Sb, contains 0.83 to 0.90 wt% As, 0.25 to 1.14 wt% Cu and 1.32 to 2.65 wt% Bi. The general chemical formula based on 13 S apfu can be calculated as: $Pb_{3.84–3.91}Bi_{0.13–0.25}Cu_{0.08–0.36}Sb_{5.50–5.79}As_{0.22–0.24}S_{12.75–12.86}$.

Semseyite displays narrow compositional ranges for the major elements Pb, Sb and S. Measurable trace elements including Fe, Cu and Bi vary from 0.08 to 0.42 wt%, 0.53 to 1.08 wt% and 0.26 to 0.36 wt%, respectively. The general chemical formula based on 21 S apfu can be calculated as: $Pb_{8.56–8.73}Fe_{0.05–0.26}Cu_{0.29–0.59}Sb_{7.89–8.03}S_{20.69–20.82}$.

Heteromorphite shows compositional variation mainly reflected in the trace elements: Fe (0.20 to 1.47 wt%), Cu (0.43 to 1.13 wt%) and Bi (0.32 to 0.50 wt%). The general chemical formula based on 19 S apfu can be calculated as: $Pb_{6.07–6.68}Fe_{0.11–0.76}Cu_{0.20–0.52}Sb_{7.86–8.02}S_{18.77–18.89}$.

Compositional variation in sphalerite, galena and chalcopyrite is limited. Galena contains minor Sb (up to 1.89 wt%). Sphalerite is conspicuously Fe-poor (0.52 to 0.98 wt%) but does contain measurable Hg (<0.17 wt%).

Minor element patterns in native gold: EPMA maps

Two morphological types of native gold are recognizable by differences in trace elements and their distribution (Fig. 3). Fine oscillatory banding with respect to Ag and Hg is noted at the grain boundaries in the coarser gold (Au1), whereas these elements are absent from the fine-grained gold (Au2). Higher concentration of Ag and Hg are noted along the grain boundaries. Bismuth, however, is evenly distributed throughout the parts of Au1 lacking any marginal Ag and Hg enrichment. Lead is instead present throughout the matrix of the Au2 aggregates. Based on these trace element patterns, it is clear there are two generations of native gold and these can be related to subtle changes in the sulfosalt assemblages.

LA-ICP-MS trace element data for sulfosalts and associated sulfides

The LA-ICP-MS dataset shows that all analyzed sulfosalts can incorporate a wide range of trace elements at concentrations exceeding 1 ppm (Table 2, Fig. 4). The concentrations of different elements do, however, vary significantly from mineral to mineral. Measurable As, Se, Ag, Te and Bi are noted in bournonite; As, Se, Ag, Cu and Bi in boulangerite; As, Se, Zn, Ag, Bi, Fe and Hg in tetrahedrite; As, Se, Ag, Cd, Te, Au, Mn, Zn and Hg in (Cu)-Pb-Bi-Sb sulfosalts; and As, Se, Ag, Cd, Mn, Ni, Cu and Zn in jamesonite.

Except for (Cu)-Pb-Bi-Sb sulfosalts, in which Au concentrations vary from 5 to 28 ppm, the mean Au concentrations in other sulfosalts and BMS are generally very low, in decreasing order: galena (2 ppm); chalcopyrite (0.7 ppm); tetrahedrite (0.3 ppm); sphalerite (0.3 ppm); boulangerite (0.2 ppm); jamesonite (0.1 ppm); and bournonite (0.1 ppm). Average Ag concentrations decrease in the order: tetrahedrite (2,666 ppm); Pb-Bi-Sb sulfosalts (2,297 ppm); boulangerite (64 ppm); jamesonite (22 ppm); galena (10 ppm); bournonite (9 ppm); chalcopyrite (3 ppm); and sphalerite (2 ppm).

Bismuth concentrations within Sb-dominant sulfosalts and BMS are generally consistent within and between samples, except for boulangerite and jamesonite where Bi varies two to three orders of magnitude across different samples. In boulangerite, the concentration of Bi displays a positive correlation with As and Ag but a marked antithetic relationship with Se, ranging from 12,250 to 14,560 ppm for Se-poor (30 to 44 ppm) spots, and only 12 to 16 ppm for Se-rich (150 to 165 ppm) spots. In jamesonite, the Bi concentration displays a positive correlation with In and an antithetic relationship with As, Se and Cd. Concentrations range from 2,475 to 8,120 ppm for Se-poor (53 to 69 ppm) spots and 14 to 16 ppm for Se-rich (122 to 127 ppm) spots.

Galena incorporates relatively high concentrations of both Bi (1,940 to 4,710 ppm) and Sb (3,010 to 17,100 ppm), as well as measurable Se (110 to 318 ppm) and Te (up to 33 ppm). We note that Sb concentrations vary greatly across the sample suite. Although low on average, measured Au concentrations in galena above 10 ppm are likely associated with mineral inclusions beneath the sample surface, based on the irregular Au signals on the time-resolved LA-ICP-MS depth profiles.

Concentrations of most trace elements in sphalerite vary greatly across the sample suite. Cadmium concentrations (317 to 4,558 ppm) tend to positively correlate with Fe. Both In and Hg display an inverse correlation with Fe content, and range between 1 to 18 ppm and 45 to 128 ppm, respectively.

The trace elements at concentrations measurable by LA-ICP-MS within chalcopyrite are Au, As, Zn and In. In all cases, the highest values for those elements are most likely associated with micro-to nanoscale inclusions, considering the irregular time-resolved signals. Other elements are typically lower than 5 ppm in chalcopyrite, if above mdl.

LA-ICP-MS element mapping

Representative assemblages containing both sulfosalts and BMS were mapped by LA-ICP-MS (Figs. 5–7 and Supplemental[3] Figures 1–3) to visualize the preferred partitioning of elements among co-existing minerals.

Assemblages of bournonite and jamesonite (Fig. 5 and Supplemental[3] Figure 1), demonstrate how Fe, Zn, Bi, Cd, Ni, Ag and In, are preferentially partitioned into jamesonite, whereas the preferred host for Cu and As is bournonite. Element distribution maps for an assemblage of jamesonite–boulangerite–sphalerite (Fig. 6) shows that jamesonite hosts Bi, whereas boulangerite primarily concentrates As, Ag, Sn, Se and Te. Cadmium and Co are enriched in sphalerite relative to the sulfosalts. Maps for a bournonite–tetrahedrite–sphalerite–chalcopyrite–native gold assemblage are shown in Fig. 7. Note here that chalcopyrite replaces tetrahedrite and is thus later. Silver, Cu, Co and Fe are mainly concentrated in tetrahedrite; As, Sb, Pb, Bi and Se occur preferentially in bournonite; and In is hosted within sphalerite. Partitioning of elements between bournonite and tetrahedrite is further confirmed in Supplemental[3] Figure 2, which also shows that, in the absence of sphalerite, Cd, Zn and Hg are mainly located within tetrahedrite.

A last map (Supplemental^3 Figure 3), including sulfosalts, BMS, and pyrite, shows that pyrite is enriched in Au and Co relative to all other phases. Tetrahedrite contains the most Ag, bournonite the highest concentrations of Bi, and sphalerite is distinguished by its enrichment in Cd.

DISCUSSION

Au and Ag concentrations in sulfosalts and BMS

Available data on equilibrium partitioning behavior between sphalerite, galena, chalcopyrite and tetrahedrite–tennantite shows that Ag is primarily hosted in the latter mineral (George et al. 2017). In contrast, concentrations and partitioning behavior of Au and Ag among different sulfosalts and between Pb-Sb sulfosalts and BMS are poorly constrained, although an association of native gold, sulfosalts and BMS is common in many gold deposits.

The measured mean Au concentration in (Cu)-Pb-Bi-Sb sulfosalts is comparable with those in Pb-Bi sulfosalts from elsewhere (Ciobanu et al. 2009). Such concentrations are in the same range as those in pyrite and arsenopyrite (mean values of ~3 and 38 ppm, respectively; Li et al. in press), the most efficient minerals to lock-in invisible gold in gold deposits (Cook and Chryssoulis 1990). This preferred Au partitioning behavior is confirmed by the elemental maps (Supplemental^3 Figure 3), showing Au hosted in pyrite. LA-ICP-MS data show that Au concentrations in other sulfosalts and BMS are generally <1 ppm, suggesting that they are poor gold carriers. Due to the low Au concentration, no striking differences are seen on the element maps (Supplemental^3 Figures 1 and 3). Hence, combined with the published data for fahlore and BMS (Ciobanu et al. 2009; Cook et al. 2009; George et al. 2016, 2017, 2018, and references therein), we conclude that (Cu)-Pb-Sb sulfosalts and BMS play negligible roles in gold distribution.

Compositional data and LA-ICP-MS element mapping further confirm that Ag is primarily hosted in sulfosalts relative to BMS. Tetrahedrite contains the highest Ag content, reflecting the fact that Ag readily enters the fahlore crystal structure (Pattrick and Hall 1983; Sack and Loucks 1985; Johnson et al. 1986). Lower temperatures and oxidized conditions are said to favor substitution of Ag for Cu in tetrahedrite (Pattrick and Hall 1983; Huston et al. 1996). We present the first data for Ag concentrations in other (Cu)-Pb-Sb sulfosalts; all are characterized by a low concentration (mostly <30 ppm). It seems that sulfosalts with higher Ag contents tend to also have higher Au concentrations (Fig. 4a), a feature which may be principally controlled by Goldschmidt's substitution rules. This also raises the question of whether Ag exhibits a similar ‘catalyst’ role for incorporation of Au in sulfosalts (Ciobanu et al. 2009), as As does in pyrite (Reich et al. 2005). Additional research is needed to constrain this.

Partitioning of other elements

Thorough petrographic and (micro) textural examinations are necessary to convincingly interpret apparent element partitioning behavior, since the effects of superimposed, non-equilibrium remobilization and overgrowth processes may significantly mask the true partitioning coefficients among minerals. In the Gutaishan deposit, the relative lack of deformation seen in quartz veins and the generally good preservation of trace element zonation patterns in pyrite and arsenopyrite (Li et al. in press) preclude significant post-crystallization re-distribution of trace element among minerals.

The correlation patterns for Bi and Ag show different trends between the different assemblages. In the jamesonite–bournonite assemblages (Fig. 5 and Supplemental[3] Figure 1), the As-deficient jamesonite hosts more Bi and Ag than coexisting bournonite. The relatively As-enriched boulangerite hosts lesser Bi but higher Ag than coexisting jamesonite (Fig. 6). Bournonite hosts more Bi but less Ag than coexisting tetrahedrite with an inhomogeneous distribution of As (Fig. 7 and Supplemental[3] Figure 2). LA-ICP-MS element maps show that Pb-Sb sulfosalts are preferred hosts for trace Bi compared to sulfides (Supplemental[3] Figure 3), consistent with trends observed for tetrahedrite (George et al. 2017).

Among BMS, LA-ICP-MS data results show that the preferred host for Ga is sphalerite, and galena incorporates higher Sb, Ag, Se and Bi (Table 2), coincident with reported relationships in chalcopyrite–

sphalerite–galena assemblages (George et al. 2016). High Bi and Sb contents in galena may be explained by Ag(Bi,Sb)S_2-PbS solid solution. The measured Sb concentrations in Gutaishan galena are generally two or more times higher than typical values measured in galena from different types of deposits (George et al. 2015). This may represent additional evidence for the high Sb content of ore-forming fluids. The LA-ICP-MS data show that galena is the preferred host for Tl (1 to 5 ppm) among all minerals, also consistent with George et al. (2015). Concentrations of Se in galena (ranging from 110 to 318 ppm) are similar to those of bournonite and boulangerite within the same sample, but always at least one order magnitude higher than in tetrahedrite. Mercury is generally <mdl in galena but measurable in sphalerite at concentrations between 45 and 128 ppm. Indium concentrations are low but the element occurs preferentially within low-Fe-sphalerite, consistent with published data (Cook et al. 2009).

Formation of high fineness native gold and implications for ore genesis

In nature, gold occurs as a metal or alloyed with silver, and gold fineness is expressed as 1000×Au/(Au+Ag) by weight. Gold fineness has practical significance for gold recovery and theoretical implications for genetic modelling (Fisher 1945; Svetlitskaya et al. 2018). Values of gold fineness for the Gutaishan deposit range from 952 to 1,000 (authors unpublished data), in good agreement with quartz vein-type gold deposits hosted within metamorphosed rocks, which are generally characterized by native gold with high and consistent fineness (Morrison et al. 1991).

To our knowledge, most studies have focused on the role played by physicochemical parameters in governing gold fineness (Morrison et al. 1991; Huston et al. 1992; Pal'yanova 2008). In contrast, few systematic studies have been conducted to investigate partitioning coefficients for Au and Ag between coexisting host phases, which may be a critical factor in controlling gold fineness (Sack and Brackebusch 2004). Together with data given by Li et al. (2016), the new information presented here enable us to evaluate the most probable factors governing formation of high-fineness native gold in the Gutaishan deposit.

(1) Measured fluid inclusion data (Li et al. 2016) indicate that ore-forming fluids were mesothermal (200 to 320 °C) with moderate- to low-salinity (0 to 13 wt% NaCl equiv.). The mineral assemblage (pyrite+ankerite) indicates that the ore-forming fluid had the capacity to transport Ag as $AgCl_2^-$and Au as $Au(HS)_2^-$(Fig. 8a) (Gammons and Williams-Jones 1995). The absence of any Ag-Sb- or Ag-Pb-Sb sulfosalts may indicate the relatively Ag-poor character of the ore-forming fluid, as the availability of Ag is the principal controlling factor, irrespective of physicochemical conditions (temperature, pH, or redox state) and the speciation of Ag in the fluid (Shikazono and Shimizu 1987). A high Au/Ag ratio in the ore-forming fluids would have contributed to the formation of high fineness native gold (Fig. 8b).

(2) Silver is mainly incorporated into minerals other than native gold. The EPMA data reveal that fahlore species at Gutaishan are close to end-member tetrahedrite, which tends to incorporate more Ag than tennantite (Wu and Petersen 1977). Although the Ag concentrations measured by LA-ICP-MS are relatively modest (2,293–2,943 ppm), scavenging by tetrahedrite may promote the formation of high-fineness native gold (Sack and Brackebusch 2004). Besides tetrahedrite, some Ag is also seen to be hosted in (Cu)-Pb-Bi-Sb sulfosalts, boulangerite and others, albeit at lower concentrations. It is therefore reasonable to link the presence of high fineness native gold with an abundance of sulfosalts, and to propose that enrichment in Sb will elevate native gold fineness in Au deposits, an interpretation consistent with data from Au–Sb deposits worldwide (e.g., Dill et al. 1995; Kontak et al. 1996).

(3) The lack of distinct homogenization temperatures for fluid inclusions within quartz from different depths in the Gutaishan system (Li et al. 2016), indicates that the effects of cooling-induced gold precipitation are insignificant. No obvious temperature decrease will keep $AgCl_2^-$ complexes in solution, permitting transport over considerable distances, a phenomenon invoked to explain distal vein-type Pb–Zn–Ag mineralization on the peripheries of porphyry-skarn deposits (Sillitoe 2010; Mao et al. 2011). Therefore, precipitation of native gold through sulfidation of wallrock (Morrison et al. 1991) may have facilitated formation of high fineness native gold in the case of the Gutaishan deposit.

There is nonetheless evidence for a later, superimposed redistribution of trace elements at local scale in the Gutaishan ores. This is shown by re-distribution of Ag in coarse-grained native gold (Au1) (Fig. 3) which is not followed by Bi. We choose to interpret these patterns as indicating either: (i) Ag/Au ratios in fluid increased during the final stages of crystallization; or (ii) remobilized silver (possibly from break-down of tetrahedrite or other minerals) reacted with native gold and diffused into the latter along grain margins. The highest Au fineness is seen in the fine-grained aggregates (Au2) which lack both Ag and Bi (Fig. 3). Nucleation of Au2 can be associated with the formation of more complex sulfosalt associations (semseyite, heteromorphite, unnamed sulfosalt; Fig. 2d). Whereas solid state diffusion can be invoked for such changes in the sulfosalt assemblage or for formation of the Ag-rich rim in Au1, formation of Au2 is instead attributable to fluid-driven reactions leading to dissolution of Au1 and reprecipitation as Au2. Arguments for this interpretation are the contrasting size and chemistry of the two gold generations, as well as the presence of minute sulfosalt grains between the Au2 aggregates.

Plausible sources for Au, Sb, Bi, and Te

The enrichment of Au, Sb, Bi, and Te in the Gutaishan deposit is difficult to explain solely by a model involving leaching of wallrock, due to the low content of these elements in fresh wallrock (<1 ppb, 0.38 to 1.25 ppm, 0.03 to 0.31 ppm, and <0.05 ppm for Au, Sb, Bi and Te respectively; Ma et al. 2002, and authors unpublished data).

Li et al. (2018) have inferred that a magmatic-hydrothermal origin for the Gutaishan deposit may be reasonable based on three lines of evidence. Firstly, available stable isotope signatures collectively indicate likely derivation from a magmatic source: ankerite with $\delta^{13}C_{PDB}$= –10.3‰ ~ –8.6‰, $\delta^{18}O_{V\text{-}SMOW}$= 13.9‰ ~ 15.7‰; fluid inclusions within quartz with $\delta^{18}O_{V\text{-}SMOW}$= 15.6‰ ~ 17.9‰, $\delta^{18}O_{H2O}$= 4.5‰ ~ 8.3‰; and arsenopyrite with $\delta^{34}S$= –2.7‰ ~ –0.7‰. Secondly, geophysical evidence suggests a hidden intrusion may exist at depth around the Gutaishan Au–Sb deposit (Rao et al. 1993). In this study, the presence of Bi, Se and Te as discrete minerals may provide additional evidence to define a magmatic signature for the Gutaishan deposit. Although the genetic link between Au-Bi-Te-(Se) mineralogy and "magmatic" signature is still a topic of debate (Ciobanu et al. 2006), the fact remains that Bi-Te-Se sulfosalts or sulfides are persistently present in intrusion-related deposits, i.e., Au skarns deposits (Meinert 2000), epithermal gold deposits (Jensen and Barton 2000) and intrusion-related gold deposits (Lang and Baker 2001).

CONCLUSIONS

The data presented allow the following conclusions to be made.

- All (Cu)-Pb-Sb sulfosalts analyzed in this study are found to be poor hosts for gold and thus do not contribute to the overall mineralogical gold balance. Trace yet measurable gold concentrations are noted in (Cu)-Pb-Bi-Sb sulfosalts, concordant with published data indicating that these minerals may be minor Au-hosts in some ore systems.
- Silver is preferentially partitioned into fahlore at the expense of other sulfosalt phases. Tetrahedrite is likely a major Ag-host in the Gutaishan deposit.
- Several partitioning relationships for minor elements among different sulfosalt and BMS phases are identified. Jamesonite is identified to preferentially incorporate Fe, Zn, Bi, Cd, Ni, Ag and In over bournonite. Boulangerite is however a better host for Ag, Sn, Se and Te than jamesonite, and will also have a higher As-component. Cadmium, Co and In are typically enriched in sphalerite relative to the sulfosalts, although Cd will be concentrated in tetrahedrite where no sphalerite is present. When present, pyrite is enriched in Au and Co relative to all other phases.
- A high Au/Ag ratio in the ore-forming fluid, the presence of abundant tetrahedrite that has sequestered silver, and the lack of evidence for precipitation driven by cooling may be significant reasons for the formation of high-fineness native gold throughout the deposit.

- Local scale remobilization is marked by (i) an increase in the complexity of sulfosalt associations; (ii) redistribution of minor elements in gold associated with the main (Cu)-Pb-Sb sulfosalts; and (iii) precipitation of a second gold generation with highest Au fineness.

ACKNOWLEDGMENTS

We would like to thank the staff at Adelaide Microscopy for assistance with microanalytical work. We are grateful to Ian Graham, an anonymous reviewer, and Associate Editor Julie Roberge for their insightful comments on our manuscript. Financial support for this study was provided by the National Basic Research Program of China (2014CB440902), the National Science Foundation of China (41573042 and 41372090), and the MNR Key Laboratory of Metallogeny and Mineral Assessment, Institute of Mineral Resources, Chinese Academy of Geological Sciences (ZS1702). Appreciation is extended to Zhiyuan Zhang, Yong Chen and Can Jiang for providing invaluable assistance during fieldwork.

REFERENCES

Abraitis, P.K., Pattrick, R.A.D., and Vaughan, D.J. (2004) Variations in the compositional, textural and electrical properties of natural pyrite: a review. International Journal of Mineral Processing, 74, 41–59.

Ciobanu, C.L., Cook, N.J., and Spry, P.G. (2006) Preface–Special Issue: telluride and selenide minerals in gold deposits–how and why? Mineralogy and Petrology, 87, 163–169.

Ciobanu, C.L., Cook, N.J., Pring, A., Brugger, J., Danyushevsky, L.V., and Shimizu, M. (2009) ‘Invisible gold’ in bismuth chalcogenides. Geochimica et Cosmochimica Acta, 73, 1970–1999.

Ciobanu, C.L., Cook, N.J., Maunders, C., Wade, B.P., and Ehrig, K. (2016) Focused ion beam and advanced electron microscopy for minerals: insights and outlook from bismuth sulphosalts. Minerals, 6, 112; doi:10.3390/min6040112

Cook, N.J., and Chryssoulis, S.L. (1990) Concentrations of "invisible gold" in the common sulfides. Canadian Mineralogist, 28, 1–16.

Cook, N.J., and Ciobanu, C.L. (2004) Bismuth tellurides and sulphosalts from the Larga hydrothermal system, Metaliferi Mts., Romania: paragenesis and genetic significance. Mineralogical Magazine, 68, 301–321.

Cook, N.J., Ciobanu, C.L., Pring, A., Skinner, W., Shimizu, M., Danyushevsky, L., Saini-Eidukat, B., and Melcher, F. (2009) Trace and minor elements in sphalerite: a LA-ICPMS study. Geochimica et Cosmochimica Acta, 73, 4761–4791.

Cook, N.J., Ciobanu, C.L., Meria, D., Silcock, D., and Wade, B. (2013) Arsenopyrite-pyrite association in an orogenic gold ore: tracing mineralization history from textures and trace elements. Economic Geology, 108, 1273–1283.

Dill, H.G., Weiser, T., Bernhardt, I.R., and Kilibarda, C.R. (1995) The composite gold-antimony vein deposit at Kharma (Bolivia). Economic Geology, 90, 51–66.

Fadda, S., Fiori, M., and Grillo, S.M. (2005) Chemical variations in tetrahedrite-tennantite minerals from the Furtei epithermal Au deposit, Sardinia, Italy: mineral zoning and ore fluids evolution. Mineralogy and Petrology, 43, 79–84.

Fisher, N.H. (1945) The fineness of gold, with special reference to the Morobe goldfield, New Guinea. Economic Geology, 40, 449–495.

Gammons, C.H., and Williams-Jones, A.E. (1995) Hydrothermal geochemistry of electrum; thermodynamic constraints. Economic Geology, 90, 420–432.

George, L., Cook, N.J., Ciobanu, C.L., and Wade, B.P. (2015) Trace and minor elements in galena: a reconnaissance LA-ICP-MS study. American Mineralogist, 100, 548–569.

George, L.L., Cook, N.J., and Ciobanu, C.L. (2016) Partitioning of trace elements in co-crystallized sphalerite–galena–chalcopyrite hydrothermal ores. Ore Geology Reviews, 77, 97–116.

George, L.L., Cook, N.J., and Ciobanu, C.L. (2017) Minor and trace elements in natural tetrahedrite-tennantite: effects on element partitioning among base metal sulphides. Minerals, 7; doi:10.3390/min7020017

George, L.L., Cook, N.J., Crowe, B.B.P., and Ciobanu, C.L. (2018) Trace elements in hydrothermal chalcopyrite. Mineralogical Magazine, 82, 59–88.

Hu, R.Z., and Zhou, M.F. (2012) Multiple Mesozoic mineralization events in South China–an introduction to the thematic issue. Mineralium Deposita, 47, 579–588.

Hu, R.Z., Fu, S.L., Huang, Y., Zhou, M.F., Fu, S.H., Zhao, C.H., Wang, Y.J., Bi, X.W., and Xiao, J.F. (2017) The giant South China Mesozoic low–temperature metallogenic domain: reviews and a new geodynamic model. Journal of Asian Earth Sciences, 137, 9–34.

Huston, D.L., Bottrill, R.S., Creelman, R.A., Zaw, K., Ramsden, T.R., Rand, S.W., Rand, S.W., Gemmell, J.B., Jablonski, W., Sie, S.H., and Large, R.R. (1992) Geologic and geochemical controls on the mineralogy and grain size of gold-bearing phases, Eastern Australian volcanic-hosted massive sulfide deposits. Economic Geology, 87, 542–563.

Huston, D.L., Jablonski, W., and Sie, S.H. (1996) The distribution and mineral hosts of silver in Eastern Australian volcanogenic massive sulfide deposits. Canadian Mineralogist, 34, 529–546.

Jensen, E.P., and Barton, M.D. (2000) Gold deposits related to alkaline magmatism. Reviews in Economic Geology, 13, 279–314.

Johnson, N.E., Craig, J.R., and Rimstidt, J.D. (1986) Compositional trends in tetrahedrite. Canadian Mineralogist, 24, 385–397.

Kontak, D.J., Horne, R.J., and Smith, P.K. (1996) Hydrothermal characterization of the West Gore Sb–Au deposit, Meguma Terrane, Nova Scotia, Canada. Economic Geology, 91, 1239–1262.

Lang, J., and Baker, T. (2001) Intrusion–related gold systems: the present level of understanding. Mineralium Deposita, 36, 477–489.

Li, W., Xie, G.Q., Zhang, Z.Y., and Zhang, X.K. (2016) Constraint on the genesis of Gutaishan gold deposit: evidence from fluid inclusion and C–H–O isotopes. Acta Petrologica Sinica, 32, 3489–3506 (in Chinese with English abstract).

Li, W., Xie, G.Q., Mao, J.W., Zhang, Z.Y., Fu, B., and Lu, S. (2018) Muscovite $^{40}Ar/^{39}Ar$ and in situ sulfur isotope analyses of the slate-hosted Gutaishan Au–Sb deposit, South China: implications for possible Late Triassic magmatic-hydrothermal mineralization. Ore Geology Reviews, 101, 839–853.

Li, W., Cook, N.J., Xie, G.Q., Mao, J.W., Ciobanu, C.L., Li, J.W., and Zhang, Z.Y. (in press) Textures and trace element signatures of pyrite and arsenopyrite from the Gutaishan Au–Sb deposit, South China. Mineralium Deposita. https://doi.org/10.1007/s00126-018-0826-0

Ma, D.S., Pan, J.Y., Xie, Q.L., and He, J. (2002) Ore source of Sb (Au) deposits in Center Hunan: I. evidences of trace elements and experimental geochemistry. Mineral Deposits, 3, 366–376 (in Chinese with English abstract).

Mao, J.W., Zhang, J.D., Pirajno, F., Ishiyama, D., Su, H.M., Guo, C.L., and Chen, Y.C. (2011) Porphyry Cu–Au–Mo–epithermal Ag–Pb–Zn–distal hydrothermal Au deposits in the Dexing area, Jiangxi Province, East China–a linked ore system. Ore Geology Reviews, 43, 203–216.

Mao, J.W., Cheng, Y.B., Chen, M.H., and Pirajno, F. (2013) Major types and time–space distribution of Mesozoic ore deposits in South China and their geodynamic settings. Mineralium Deposita, 48, 267–294.

Meinert, L.D. (2000) Gold in skarns related to epizonal intrusions. Reviews in Economic Geology, 13, 347–375.

Moëlo, Y., Makovicky, E., Mozgova, N.N., Jambor, J.L., Cook, N.J., Pring, A., Paar, W., Nickel, E.H., Graeser, G., Karup-Møller, S., Balic-Žunic, T., Mumme, W.G., Vurro, F., Topa, D., Bindi, L., Bente, K., and Shimizu, M. (2008) Sulfosalt systematics: a review. Report of the Sulfosalt Sub-Committee of the IMA Commission on Ore Mineralogy. European Journal of Mineralogy, 20, 7–46.

Morrison, G.W., Rose, W.J., and Jaireth, S. (1991) Geological and geochemical controls on the silver content (fineness) of gold in gold-silver deposits. Ore Geology Reviews, 6, 333–364.

Pal'yanova, G. (2008) Physicochemical modeling of the coupled behaviour of gold and silver in hydrothermal processes: gold fineness, Au/Ag ratios and their possible implications. Chemical Geology, 255, 399–413.

Pattrick, R.A., and Hall, A.J. (1983) Silver substitution into synthetic zinc, cadmium and iron tetrahedrites. Mineralogical Magazine, 47, 441–451.

Peng, B., Piestrzynski, A., and Chen, G.H. (2000) Super-pure native gold in W–Sb–Au ores from the Woxi deposit in Western Hunan Province, China. Geotectonica et Metallogenia, 24, 51–56 (in Chinese with English abstract).

Phillips, G.N., and Powell, R. (2010). Formation of gold deposits: a metamorphic devolatilization model. Journal of Metamorphic Geology, 28, 689–718.

Rao, J.R., Wang, J.H., and Cao, Y.Z. (1993) Deep structure in Hunan. Hunan Geology, 12, 1–101 (in Chinese with English abstract).

Reich, M., Kesler, S.E., Utsunomiya, S., Palenik, C.S., Chryssoulis, S.L., and Ewing, R. (2005) Solubility of gold in arsenian pyrite. Geochimica et Cosmochimica Acta, 69, 2781–2796.

Sack, R.O., and Brackebusch, F.W. (2004) Fahlore as an indicator of mineralization temperature and gold fineness. Canadian Mining and Metallurgical Bulletin, 97, 78–83.

Sack, R.O., and Loucks, R.R. (1985) Thermodynamic properties of tetrahedrite–tennantites; constraints on the interdependence of the Ag↔Cu, Fe↔Zn, Cu↔Fe, and As↔Sb exchange reactions. American Mineralogist, 70, 1270–1289.

Shikazono, N., and Shimizu, M. (1987) The Ag/Au ratio of native gold and electrum and the geochemical environment of gold vein deposits in Japan. Mineralium Deposita, 22, 309–314.

Sillitoe, R.H. (2010) Porphyry copper systems. Economic Geology, 105, 3–41.

Svetlitskaya, T.V., Nevolko, P.A., Kolpakov, V.V., and Tolstykh, N.D. (2018) Native gold from the Inagli Pt–Au placer deposit (the Aldan Shield, Russia): geochemical characteristics and implications for possible bedrock sources. Mineralium Deposita, 53, 323–338.

Tooth, B., Brugger, J., Ciobanu, C.L., and Liu, W. (2008) Modeling of gold scavenging by bismuth melts coexisting with hydrothermal fluids. Geology, 36, 815–818.

Wagner, T., and Jonsson, E. (2001) Mineralogy of sulfosalt-rich vein-type ores, Boliden massive sulfide deposit, Skellefte district, Northern Sweden. Canadian Mineralogist, 39, 855–872.

Wu, I., and Petersen, U. (1977) Geochemistry of tetrahedrite and mineral zoning at Casapalca, Peru. Economic Geology, 72, 993–1016.

Xie, G.Q., Mao, J.W., Bagas, L., Fu, B., and Zhang, Z.Y. (2018) Mineralogy and titanite geochronology of the Caojiaba W deposit, Xiangzhong metallogenic province, southern China: Implications for a distal reduced skarn W formation. Mineralium Deposita, https://doi.org/10.1007/s00126-018-0816-2

Zhu, Y.N., and Peng, J.T. (2015) Infrared microthermometric and noble gas isotope study of fluid inclusions in ore minerals at the Woxi orogenic Au–Sb–W deposit, Western Hunan, South China. Ore Geology Reviews, 65, 55–69.

FIGURE CAPTIONS

FIGURE 1. Hand specimen photographs showing the occurrence of sulfosalt minerals in auriferous quartz veins. (a) Assemblage of bournonite (Bnn) and galena (Gn) as patches intergrown with native gold (Au). (b) Assemblage of bournonite and boulangerite (Bou) associated with coarse-grained native gold. (c) Tetrahedrite (Ttr) within quartz veins, coexisting with ankerite (Ank) and chalcopyrite (Ccp). (d) (Cu)-Pb-Bi-Sb sulfosalts coexisting with native gold. (e) Semi-massive sphalerite (Sp) intergrown with jamesonite (Ja) and boulangerite.

FIGURE 2. Representative BSE images showing aspects of sulfosalt mineralogy. (a) Euhedral bournonite (Bnn) intergrown with sphalerite (Sp), tetrahedrite (Ttr) and native gold (Au1). Native gold is enclosed by galena (Gn), and chalcopyrite (Ccp) replaces tetrahedrite. This assemblage occurs as patches within quartz veins. (b) Bournonite intergrown with jamesonite (Ja), showing direct contact of both minerals with coarse native gold (Au1). Note that Au1 is homogeneous and surrounded by a porous rim (Au2). (c) Complex assemblage comprising bournonite (Bnn), boulangerite (Bou), jamesonite (Ja) and robinsonite (Rob). Acicular robinsonite and anhedral jamesonite are enclosed in bournonite. (d) Detail of area shown in b, with heteromorphite (Het), semseyite (Sem) and a third, unidentified Pb-Sb-S phase at contact between jamesonite and bournonite. (e) Prismatic boulangerite (Bou). (f) Mineral assemblage showing the relationship between bournonite, galena and chalcopyrite. (g) Co-existing bournonite, arsenopyrite (Apy) and coarse native gold (Au1).

FIGURE 3. EPMA map of an aggregate of native gold, in which the margins of individual gold grains are richer in Ag and Hg, corresponding to darker areas on the BSE image (bottom left). Units on scale are arbitrary.

FIGURE 4. Binary plots of trace elements in sulfosalts and BMS, showing the range of absolute concentrations and key inter-element relationships. (a) Au *vs.* Ag. (b) Au *vs.* Sb. (c) Bi *vs.* As. (d) Ag *vs.* As. (e) Ag *vs.* Bi. (f) Ag *vs.* Sb. Bnn=bournonite, Bou=boulangerite, Ccp=chalcopyrite, Gie/Izok=giessenite-izoklakeite, Gn=galena, Ja=jamesonite, Sp=sphalerite, Ttr=tetrahedrite.

FIGURE 5. LA-ICP-MS element maps of an assemblage comprising bournonite (Bnn) and jamesonite (Ja). Scales in counts-per-second.

FIGURE 6. LA-ICP-MS element maps of an assemblage comprising boulangerite (Bou), jamesonite (Ja) and sphalerite (Sp). Scales in counts-per-second.

FIGURE 7. LA-ICP-MS element maps of an assemblage comprising bournonite (Bnn), tetrahedrite (Ttr) and sphalerite (Sp). Small particles of native gold (Au) and chalcopyrite (Ccp) are also present. Scales in counts-per-second.

FIGURE 8. (a) Gold solubility expressed on a log$f$O$_2$ *vs.* pH diagram based on Phillips and Powell (2010). (b) Variation in gold fineness with temperature in equilibrium with fluids with different Au/Ag ratios, after Pal'yanova (2008). Grey regions incorporate data from this study.

SUPPLEMENTAL MATERIAL

Supplemental^1

TABLE S1. Elements analyzed, peak/background positions, count times, standards used and average minimum limits of detection for sulfosalts analysis by EPMA

TABLE S2. Elemental overlap corrections used in sulfide package (EPMA)

TABLE S3. Average minimum detection limits and dwell time for LA-ICP-MS spot analysis and mapping

Supplemental^2

TABLE S1. Full EPMA datasets for sulfosalts and BMS from the Gutaishan deposit

TABLE S2. Full LA-ICP-MS datasets for sulfosalts and BMS from the Gutaishan deposit

Supplemental^3

FIGURE 1. LA-ICP-MS element maps of an assemblage of bournonite (Bnn) and jamesonite (Ja). Scales in counts-per-second.

FIGURE 2. LA-ICP-MS element maps of an assemblage of bournonite (Bnn), tetrahedrite (Ttr) and galena (Gn). Scales in counts-per-second.

FIGURE 3. LA-ICP-MS element maps of an assemblage of bournonite (Bnn), tetrahedrite (Ttr), sphalerite (Sp), pyrite (Py) and chalcopyrite (Ccp). Scales in counts-per-second.

DOI: https://doi.org/10.2138/am-2019-6674

TABLE 1. Representative EPMA results of (Cu)-Pb-Sb sulfosalts and BMS from the Gutaishan deposit (data in wt%)

	Bournonite		Tetrahedrite		Boulangerite		Robinsonite		Jamesonite		Heteromorphite		Semseyite		Galena		Sphalerite		Chalcopyrite	
sample	110-2	201-7	221-2	221-3	209-3	209-11	233-10	233-11	110-6	213-1	115-1	115-2	115-4	115-5	134-3	134-7	221-9	221-10	134-4	209-6
S	19.48	19.74	25.64	25.71	18.11	18.24	20.60	20.77	21.76	21.86	20.25	20.57	19.27	19.40	13.28	13.52	32.79	32.73	35.34	35.63
Pb	41.29	40.71	0.10	<mdl	53.97	54.13	40.78	40.09	38.93	38.20	46.59	44.89	51.36	51.54	86.01	86.15	0.10	0.08	<mdl	<mdl
As	0.77	0.38	0.58	0.52	0.72	0.81	0.88	0.90	0.82	0.70	<mdl	<mdl	<mdl	<mdl	<mdl	<mdl	<mdl	<mdl	<mdl	<mdl
Fe	<mdl	0.39	0.61	0.58	<mdl	0.05	<mdl	<mdl	2.64	2.53	0.20	0.78	0.41	0.42	0.04	<mdl	0.52	0.63	30.18	29.90
Cu	13.25	13.08	38.53	38.60	<mdl	0.32	0.60	0.25	0.11	0.06	0.66	1.13	0.54	0.53	0.15	<mdl	0.06	<mdl	34.62	34.19
Sb	25.03	24.72	27.82	27.95	26.36	26.35	35.46	35.51	35.35	35.93	32.84	32.67	28.30	28.33	<mdl	0.92	0.04	<mdl	<mdl	<mdl
Bi	<mdl	<mdl	<mdl	<mdl	<mdl	<mdl	1.32	1.80	0.29	<mdl	0.50	0.32	0.36	0.26	<mdl	<mdl	<mdl	<mdl	<mdl	<mdl
Hg	<mdl	<mdl	0.12	<mdl	0.16	<mdl	0.20	0.12	<mdl	<mdl	n	n	n	n	0.12	<mdl	<mdl	<mdl	<mdl	0.12
Zn	<mdl	<mdl	7.16	7.24	<mdl	<mdl	<mdl	<mdl	0.05	0.05	<mdl	<mdl	<mdl	<mdl	<mdl	<mdl	66.59	66.85	0.06	<mdl
Se	<mdl	0.04	<mdl	<mdl	<mdl	<mdl	<mdl	<mdl	<mdl	<mdl	<mdl	0.05	0.04	<mdl	0.04	<mdl	<mdl	0.04	<mdl	<mdl
Ag	<mdl	<mdl	0.34	0.34	<mdl	<mdl	<mdl	<mdl	<mdl	<mdl	<mdl	<mdl	<mdl	<mdl	<mdl	<mdl	<mdl	<mdl	<mdl	<mdl
Te	<mdl	<mdl	<mdl	<mdl	<mdl	<mdl	<mdl	<mdl	<mdl	<mdl	0.06	<mdl	<mdl	<mdl	<mdl	<mdl	<mdl	<mdl	<mdl	<mdl
Cd	<mdl	<mdl	<mdl	<mdl	<mdl	<mdl	<mdl	<mdl	<mdl	<mdl	0.11	<mdl	<mdl	0.08	0.12	<mdl	<mdl	<mdl	<mdl	<mdl
Total	99.82	99.06	100.90	101.10	99.31	99.90	99.84	99.47	99.94	99.33	101.20	100.44	100.32	100.60	99.76	100.62	100.22	100.36	100.21	99.89
Calculated formulae																				
S	2.96	2.99	13.12	13.13	10.74	10.70	12.75	12.86	13.92	14.00	18.77	18.80	20.78	20.82	0.99	1.00	1.00	0.99	2.01	2.03
Pb	0.97	0.96	0.01	-	4.95	4.91	3.91	3.84	3.85	3.79	6.68	6.35	8.57	8.56	0.99	0.98	0.01	0.01	-	-
As	0.05	0.02	0.13	0.11	0.18	0.20	0.23	0.24	0.22	0.19	-	-	-	-	-	-	-	-	-	-
Fe	-	0.03	0.18	0.17	-	0.02	-	-	0.97	0.93	0.11	0.41	0.25	0.26	0.01	-	0.01	0.01	0.99	0.98
Cu	1.02	1.00	9.95	9.94	-	0.09	0.19	0.08	0.04	0.02	0.31	0.52	0.29	0.29	0.01	-	0.01	-	1.00	0.98
Sb	1.00	0.99	3.75	3.76	4.11	4.07	5.78	5.79	5.95	6.06	8.02	7.86	8.03	8.01	-	0.02	0.01	-	-	-
Bi	-	-	-	-	-	-	0.13	0.17	0.03	-	0.07	0.04	0.06	0.04	-	-	-	-	-	-
Hg	-	-	0.01	-	0.01	-	0.02	0.01	-	-	n	n	n	n	0.01	-	-	-	-	0.01
Zn	-	-	1.80	1.81	-	-	-	-	0.01	0.01	-	-	-	-	-	-	0.99	0.99	0.01	-
Se	-	0.01	-	-	-	-	-	-	-	-	-	0.02	0.02	-	0.01	-	-	0.01	-	-
Ag	-	-	0.05	0.05	-	-	-	-	-	-	-	-	-	-	-	-	-	-	-	-
Te	-	-	-	-	-	-	-	-	-	-	0.01	-	-	-	-	-	-	-	-	-
Cd	-	-	-	-	-	-	-	-	-	-	0.03	-	-	0.02	0.01	-	-	-	-	-

Note: Chemical formulae are calculated based on 3 S atoms for bournonite, 13 S for tetrahedrite, 11 S for boulangerite, 14 S for jamesonite, 13 S for robinsonite, 19 S for heteromorphite, 21 S for semseyite, 1S for galena and sphalerite. and 2 S for chalcopyrite. <mdl: below minimum limit of detection, n: not analyzed.

TABLE 2. LA-ICP-MS trace element data for sulfosalts and BMS from the Gutaishan deposit (data in ppm)

Mineral			Ag	Au	As	Se	Cd	In	Sn	Te	Tl	Bi	Zn	Fe	Mn	Co	Ni	Cu	Ga	Mo	Hg	Sb$^{\#}$
Bournonite	n=24	mean	9.00	0.15	4,409	115	*	*	0.69	7.79	0.30	1,402	106	29.5	*	*	*	132,016	*	*	*	243,813
		max	30.9	0.19	11,890	240	*	*	1.15	27.5	0.48	3,015	194	29.5	*	*	*	132,400	*	*	*	304,400
		min	*	*	944	55.6	*	*	*	0.88	0.11	172	*	*	*	*	*	131,400	*	*	*	198,000
		std. dev.	10.1	0.03	3,282	54.8	*	*	0.34	9.31	0.11	823	47.2	-	*	*	*	317	*	*	*	29,890
Tetrahedrite	n=7	mean	2,666	0.34	7,720	6.37	134	2.50	*	*	0.05	183	88,686	5,644	*	6.53	4.70	386,800	*	*	24.1	306,271
		max	2,943	0.50	11,570	8.90	155	3.03	*	*	0.05	246	93,300	6,080	*	7.37	4.70	386,800	*	*	34.0	369,800
		min	2,293	*	6,290	*	124	2.02	*	*	*	*	86,200	5,100	*	5.71	*	386,800	*	*	20.5	237,400
		std. dev.	285	0.14	1,781	1.67	10.9	0.44	*	*	0.01	57.4	2,374	355	*	0.75	*	0	*	*	4.62	60,392
Boulangerite	n=14	mean	64.1	0.22	2,619	91.5	1.41	0.80	5.64	6.62	0.76	6,940	159	*	*	0.92	6.29	34.5	0.14	0.05	*	231,329
		max	159	0.41	5,480	165	4.28	3.36	6.96	10.6	1.69	14,560	770	*	*	2.70	21.8	98.0	0.29	0.05	*	291,000
		min	12.7	*	727	30.1	*	*	*	*	0.37	12.1	*	*	*	*	*	*	*	*	*	203,100
		std. dev.	45.6	0.11	1,589	56.6	1.42	1.16	2.53	4.40	0.43	6,729	273	*	*	1.19	7.83	29.5	0.12	0.01	*	28,334
Giessenite-Izoklakeite	n=4	mean	2,297	11.2	628	662	320	3.22	*	635	1.15	189,800	238	*	8,230	3.41	22.0	11,683	*	0.33	65.1	68,275
		max	3,220	27.8	879	774	371	12.0	*	701	1.59	199,800	840	*	22,500	6.50	42.0	12,750	*	0.51	93.5	75,000
		min	1,503	5.08	487	610	296	0.07	*	553	0.66	184,600	19.7	*	*	*	*	9,540	*	*	46.3	64,400
		std. dev.	705	11.1	172	76.2	34.9	5.86	*	66.7	0.42	6,845	402	*	12,372	4.37	28.2	1,456	*	0.25	20.2	4,660
Jamesonite	n=31	mean	27.4	0.30	294	65.0	97.7	7.66	1.76	1.78	0.13	3,897	533	24,939	15.7	0.91	106	601	*	0.16	2.00	301,661
		max	136	0.70	948	127	430	20.8	3.85	6.03	0.17	14,520	619	29,210	43.0	2.78	1,029	5,700	*	0.30	3.33	328,100
		min	*	*	149	29.6	32.9	*	*	*	*	13.6	*	17,010	*	*	*	*	*	*	*	286,50

																						0
		std. dev.	41.9	0.19	174	24.5	122	5.56	0.76	2.53	0.02	3,033	45.0	2,223	7.22	0.54	248	1,145	*	0.11	0.79	10,997
Sphalerite	n=11	mean	1.52	0.30	1.83	1.47	2,233	8.15	0.17	*	*	0.32	664,618	15,362	17.5	15.6	0.47	50.6	10.6	*	76.7	41.8
		max	3.15	0.65	2.88	5.80	4,558	17.6	0.52	*	*	1.27	667,200	25,880	76.1	29.0	0.55	94.0	51.8	*	128	125
		min	*	*	*	*	317	1.00	0.05	*	*	*	663,100	*	1.77	5.09	*	*	*	*	45.0	*
		std. dev.	0.79	0.19	0.75	1.86	2,010	6.83	0.13	*	*	0.54	1,507	7,988	24.5	8.47	0.10	32.2	18.7	*	30.1	47.8
Galena	n=17	mean	10.4	1.69	4.66	206	1.48	0.18	*	15.4	1.94	2,966	*	*	*	*	1.33	170	*	0.58	*	9,667
		max	26.2	8.10	9.00	318	2.80	0.23	*	33.0	5.38	4,710	*	*	*	*	9.90	277	*	0.97	*	17,100
		min	1.02	*	*	110	*	*	*	*	0.76	1,940	*	*	*	*	*	*	*	*	*	3,010
		std. dev.	8.24	2.56	2.49	78.5	0.79	0.05	*	12.9	1.59	898	*	*	*	*	2.52	61.9	*	0.55	*	5,653
Chalcopyrite	n=17	mean	2.79	0.73	67.0	*	1.70	5.26	1.10	0.92	0.07	*	17.9	300,400	1.17	*	0.39	323,682	*	0.21	*	*
		max	4.73	2.01	220	*	4.80	11.8	4.58	1.09	0.19	*	30.9	300,400	1.76	*	0.90	345,000	*	0.36	*	*
		min	*	*	*	*	*	*	*	*	*	*	*	300,400	*	*	*	313,900	*	*	*	*
		std. dev.	2.13	0.50	76.5	*	1.70	4.91	1.45	0.27	0.06	*	7.44	0	0.60	*	0.30	7,626	*	0.10	*	*

Note: * signifies that measured data are either below the minimum detection limits or unreliable due to bad time-resolved signals. Internal calibration used measured wt. % EPMA data: Fe served for chalcopyrite; Cu for tetrahedrite and bournonite; values of Pb for giessenite-izoklakeite, jamesonite, robinsonite, boulangerite and galena are 48.98 wt%, 38.82 wt%, 40.40 wt%, 53.87 wt% and 85.91 wt%, respectively; Zn for sphalerite. $Sb^{\#}$ is a major element in many sulfosalts; the degree of correspondence between EPMA and LA-ICP-MS data is reasonable but not perfect in all cases, as is common when using a reference material containing trace amounts of a given element to measure major element concentrations.

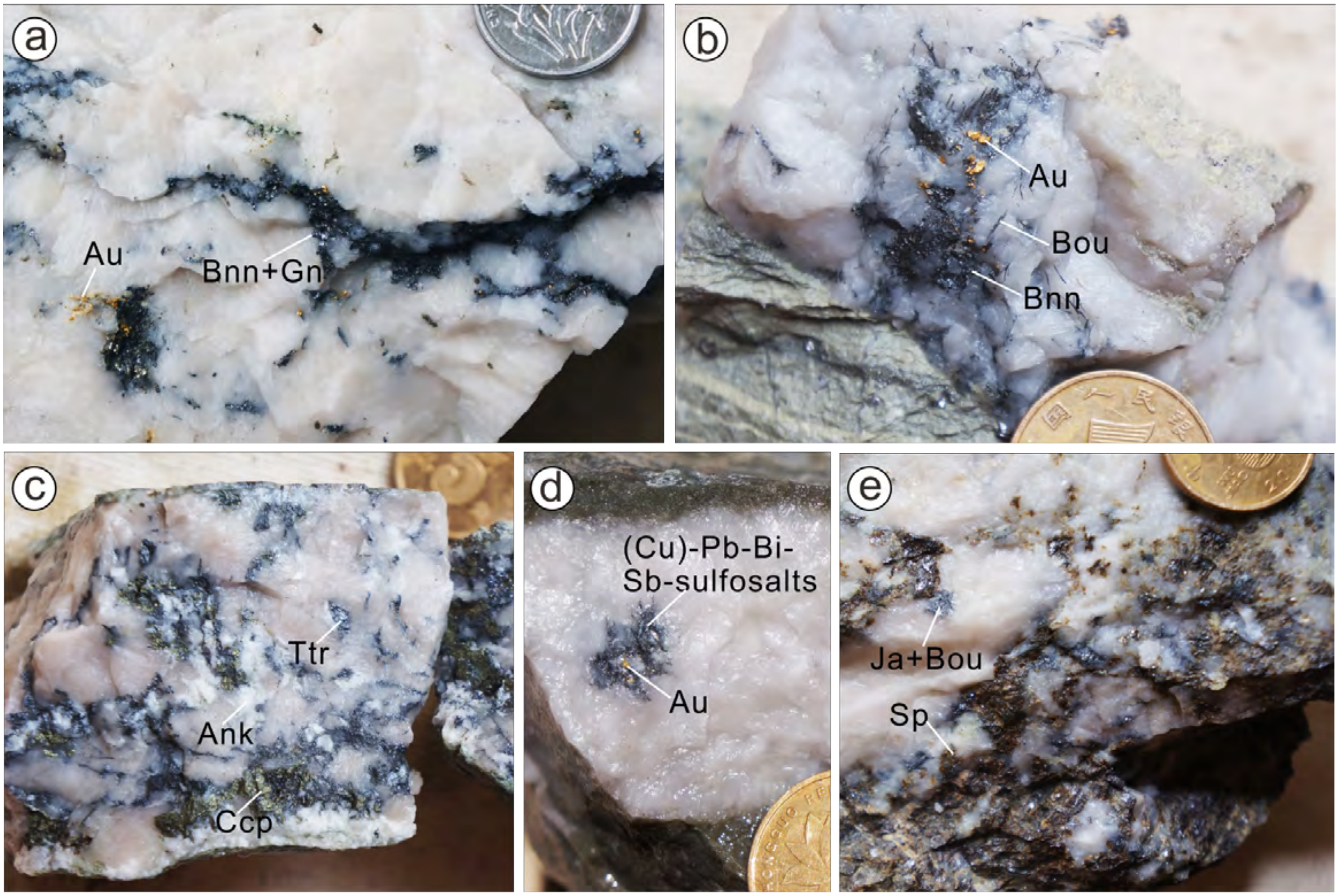
a
Au
Bnn+Gn
b
Au
Bou
Bnn
c
Ttr
Ank
Ccp
d
(Cu)-Pb-Bi-
Sb-sulfosalts
Au
e
Ja+Bou
Sp

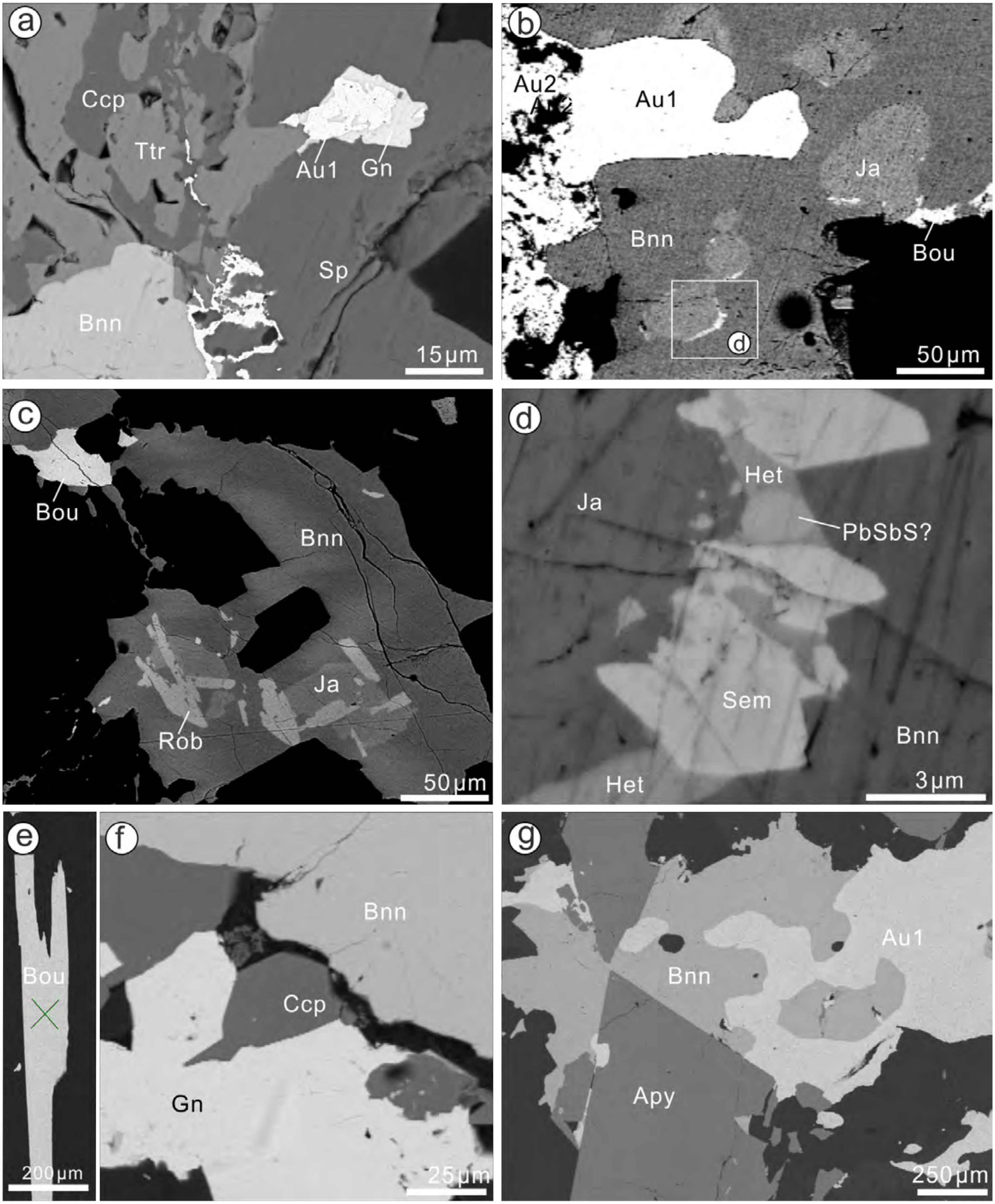
a
Ccp
Ttr
Au1
Gn
Sp
Bnn
15μm
b
Au2
Au1
Ja
Bnn
Bou
d
50μm
c
Bou
Bnn
Ja
Rob
50μm
d
Het
Ja
PbSbS?
Sem
Bnn
Het
3μm
e
Bou
200μm
f
Bnn
Ccp
Gn
25μm
g
Au1
Bnn
Apy
250μm

DOI: https://doi.org/10.2138/am-2019-6674

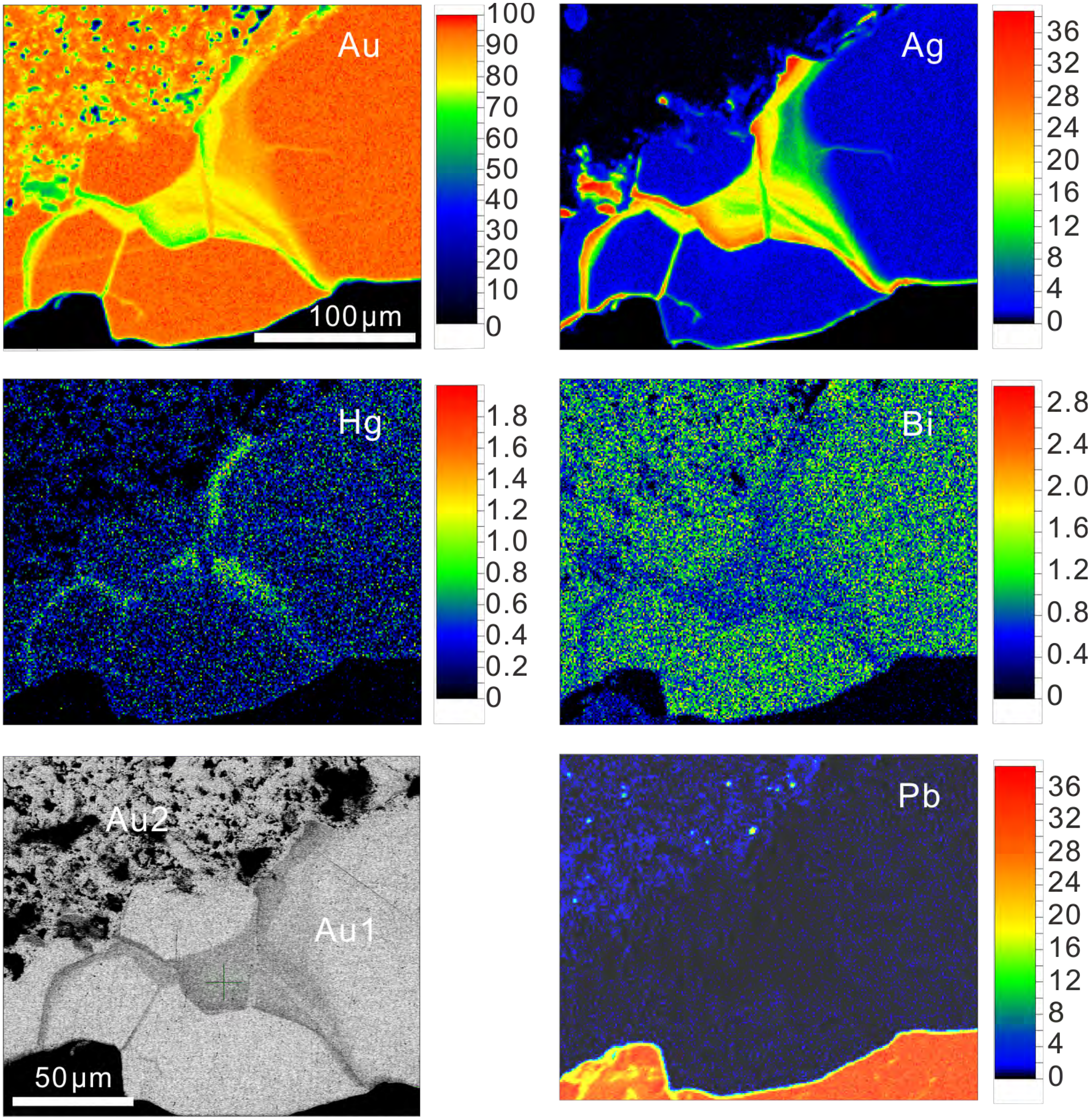

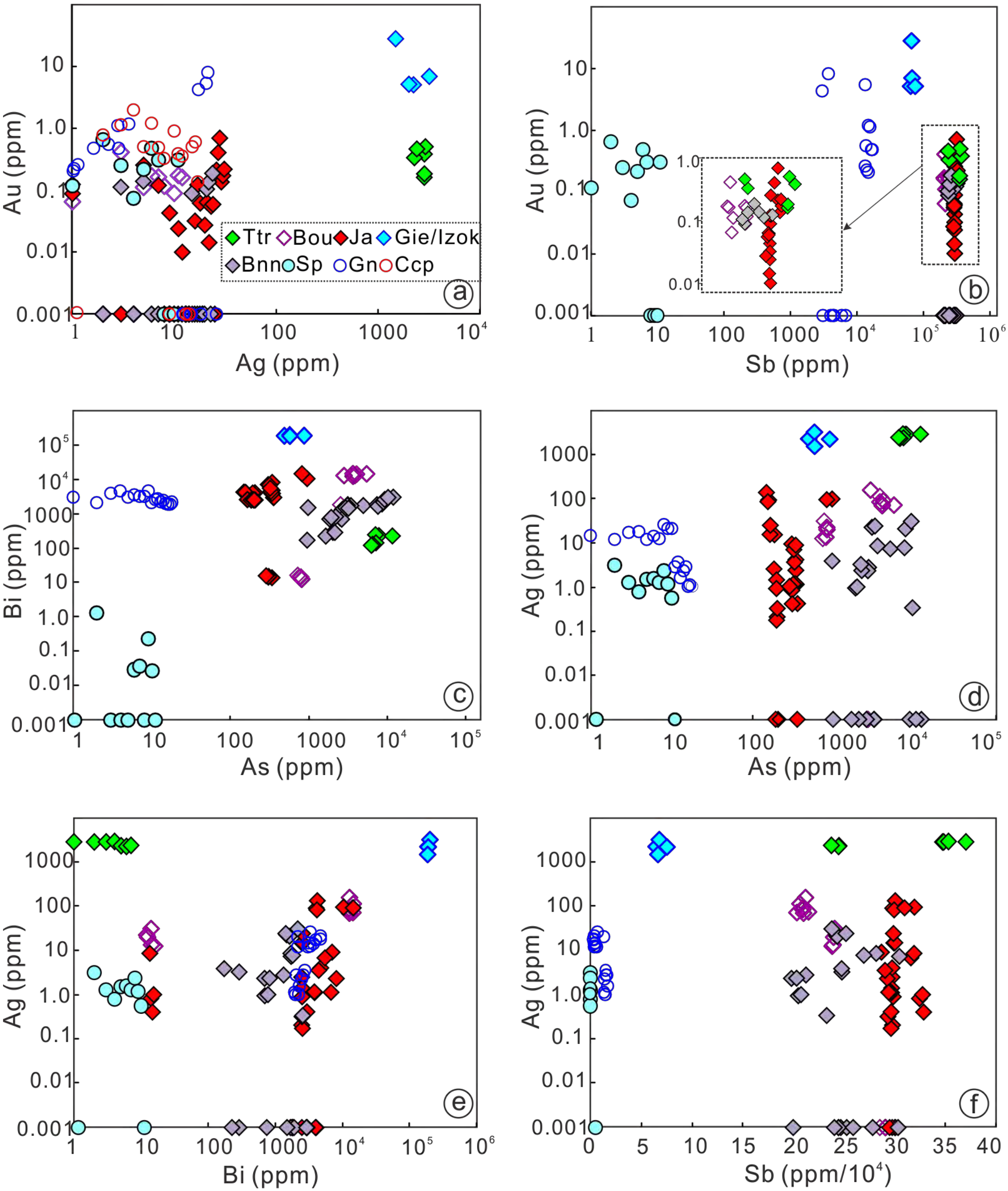
Au (ppm)
Ag (ppm)
a
Ttr
Bou
Ja
Gie/Izok
Bnn
Sp
Gn
Ccp
Au (ppm)
Sb (ppm)
b
Bi (ppm)
As (ppm)
c
Ag (ppm)
As (ppm)
d
Ag (ppm)
Bi (ppm)
e
Ag (ppm)
Sb (ppm/10⁴)
f

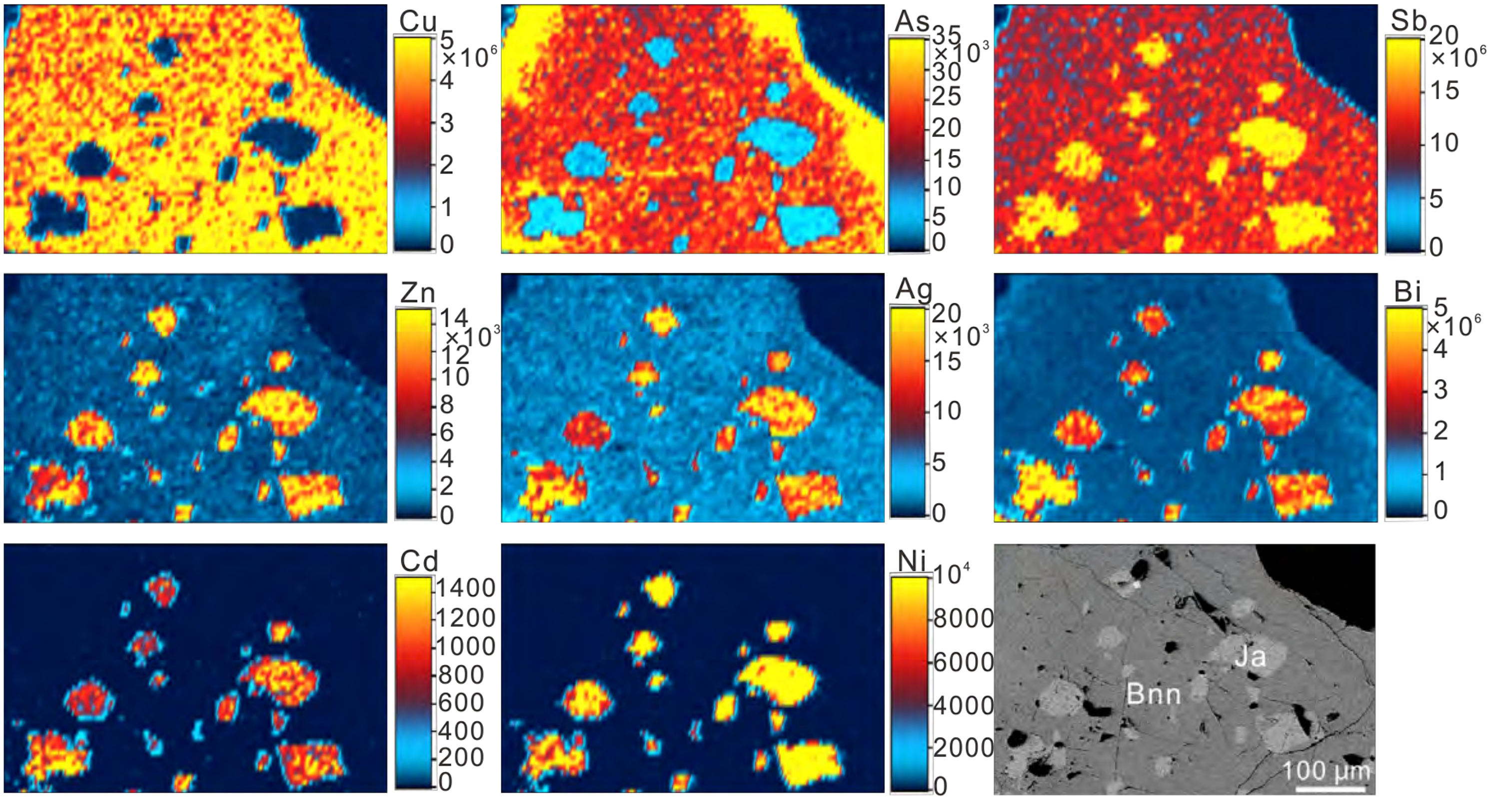
Cu
5
×10^6
4
3
2
1
0
As
35
×10^3
30
25
20
15
10
5
0
Sb
20
×10^6
15
10
5
0
Zn
14
×10^3
12
10
8
6
4
2
0
Ag
20
×10^3
15
10
5
0
Bi
5
×10^6
4
3
2
1
0
Cd
1400
1200
1000
800
600
400
200
0
Ni
10^4
8000
6000
4000
2000
0
Ja
Bnn
100 μm

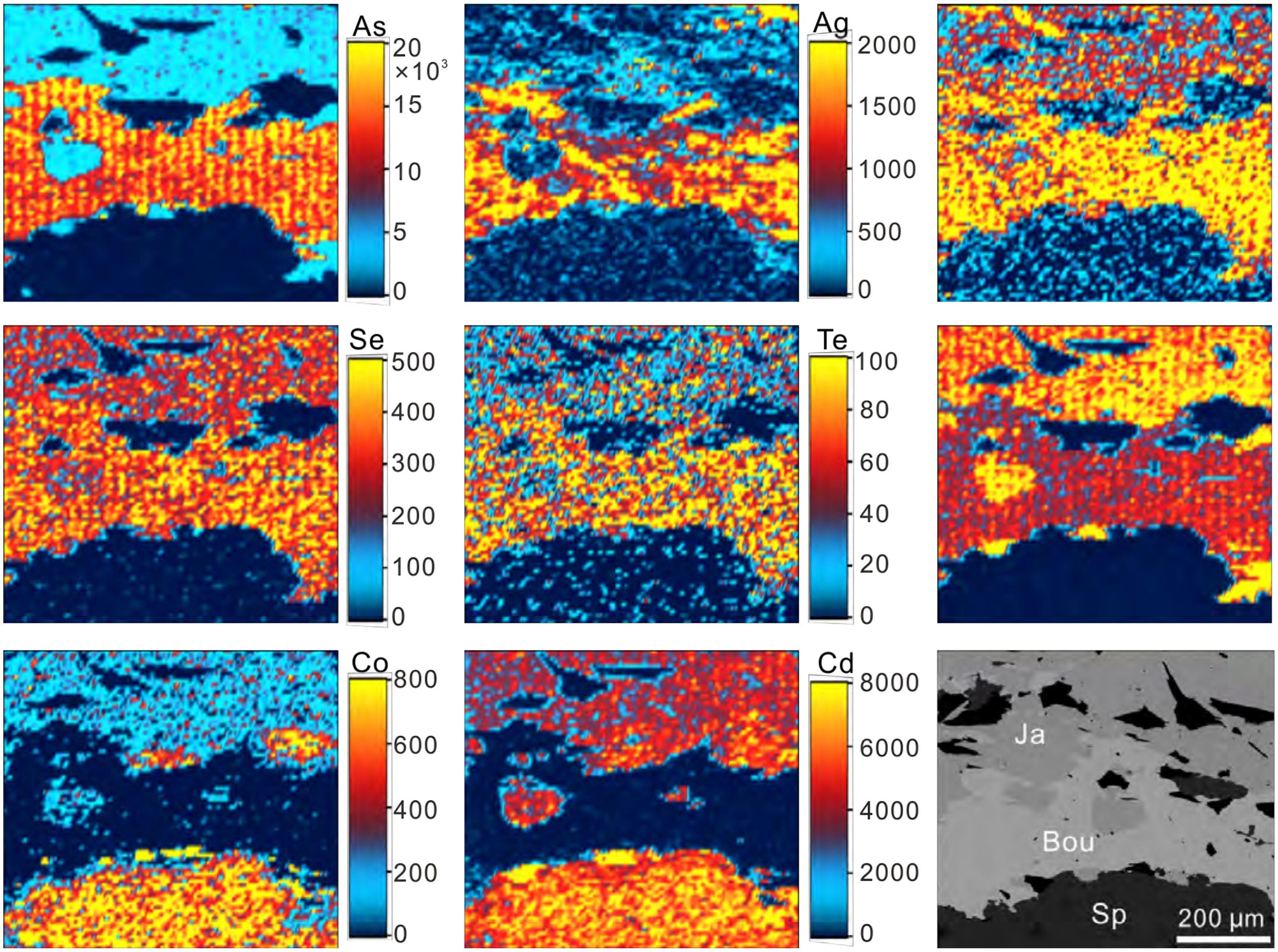
As
20 ×10³
15
10
5
0
Ag
2000
1500
1000
500
0
Sn
500
400
300
200
100
0
Se
500
400
300
200
100
0
Te
100
80
60
40
20
0
Bi
8000
6000
4000
2000
0
Co
800
600
400
200
0
Cd
8000
6000
4000
2000
0
Ja
Bou
Sp
200 μm

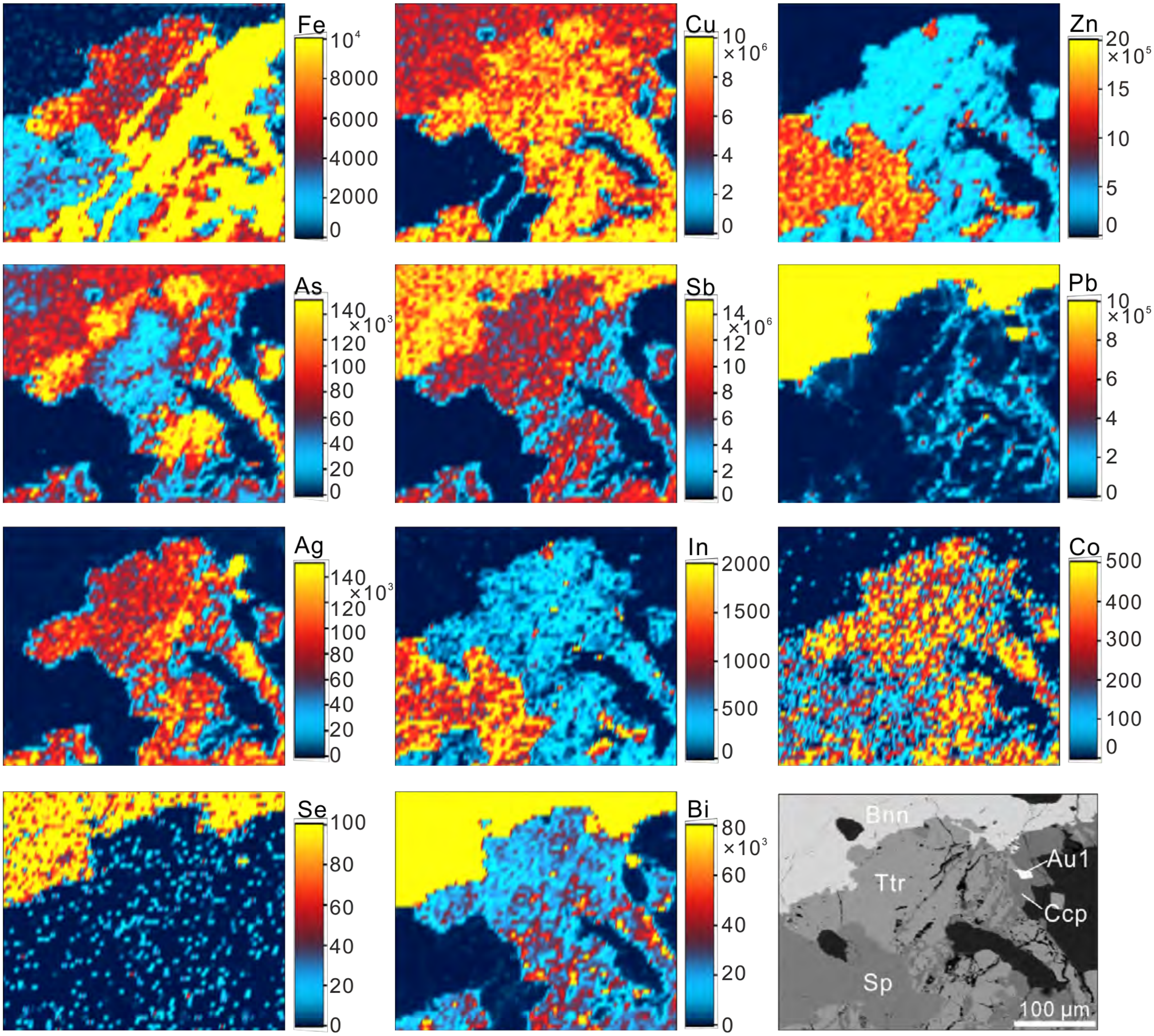
Fe
10^4
8000
6000
4000
2000
0
Cu
10
$\times10^6$
8
6
4
2
0
Zn
20
$\times10^5$
15
10
5
0
As
140
$\times10^3$
120
100
80
60
40
20
0
Sb
14
$\times10^6$
12
10
8
6
4
2
0
Pb
10
$\times10^5$
8
6
4
2
0
Ag
140
$\times10^3$
120
100
80
60
40
20
0
In
2000
1500
1000
500
0
Co
500
400
300
200
100
0
Se
100
80
60
40
20
0
Bi
80
$\times10^3$
60
40
20
0
Bnn
Au1
Ttr
Ccp
Sp
100 μm

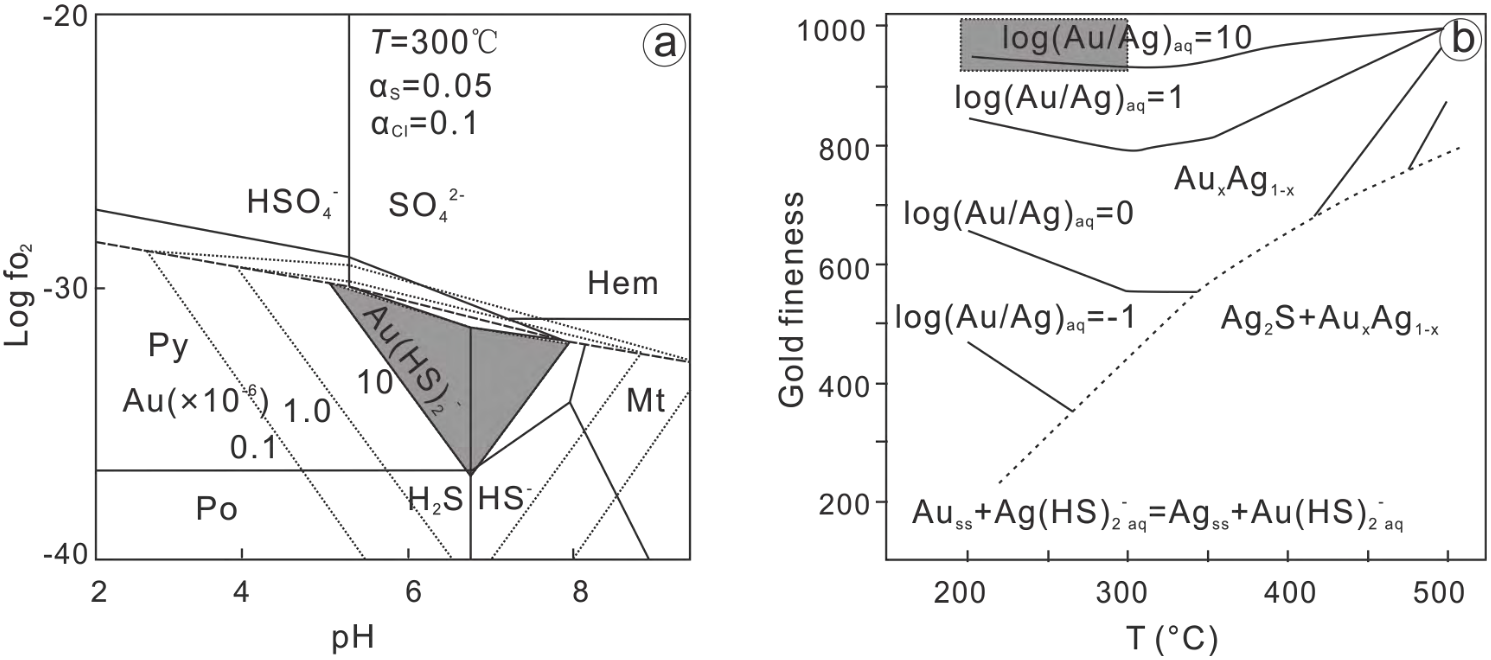
a
T=300℃
α_S=0.05
α_{Cl}=0.1
HSO$_4^-$
SO$_4^{2-}$
Hem
Py
Au(HS)$_2^-$
10
Au(×10^{-6})
1.0
0.1
Mt
Po
H$_2$S
HS$^-$
Log fo$_2$
-20
-30
-40
2
4
6
8
pH
b
log(Au/Ag)$_{aq}$=10
log(Au/Ag)$_{aq}$=1
Au$_x$Ag$_{1-x}$
log(Au/Ag)$_{aq}$=0
log(Au/Ag)$_{aq}$=-1
Ag$_2$S+Au$_x$Ag$_{1-x}$
Au$_{ss}$+Ag(HS)$_2^-$$_{aq}$=Ag$_{ss}$+Au(HS)$_2^-$$_{aq}$
Gold fineness
1000
800
600
400
200
200
300
400
500
T (°C)